29th International Conference
ENGINEERING MECHANICS 2023
Milovy, Czech Republic, May 9 – 11, 2023

SIMULATING PARTICLE-LADEN FLOWS: FROM IMMERSED BOUNDARIES TOWARDS MODEL ORDER REDUCTION

Isoz M.[*], **Kubíčková L.**[**], **Kotouč Šourek M.**[***], **Studeník O.**[†], **Kovárnová A.**[‡]

Abstract: *Particle-laden flow is prevalent both in nature and in industry. Its appearance ranges from the transport of riverbed sediments towards the magma flow; from the deposition of catalytic material inside particulate matter filters in automotive exhaust gas aftertreatment towards the slurry transport in dredging operations. In this contribution, we focus on the particle-resolved direct numerical simulation (PR-DNS) of the particle-laden flow. Such a simulation combines the standard Eulerian approach to computational fluid dynamics (CFD) with inclusion of particles via a variant of the immersed boundary method (IBM) and tracking of the particles movement using a discrete element method (DEM). Provided the used DEM allows for collisions of arbitrarily shaped particles, PR-DNS is based (almost) entirely on first principles, and as such it is a truly high-fidelity model. The downside of PR-DNS is its immense computational cost. In this work, we focus on three possibilities of alleviating the computational cost of PR-DNS: (i) replacing PR-DNS by PR-LES or PR-RANS, while the latter requires combining IBM with wall functions; (ii) improving efficiency of DEM contact solution via adaptively refined virtual mesh; and (iii) developing a method of model order reduction specifically tailored to PR-DNS of particle-laden flows.*

Keywords: particle-laden flow, CFD-DEM, arbitrarily-shaped particles, finite volume method.

1. Introduction

Processes with a solid phase dispersed in a fluid are omnipresent in both nature and industry. Just a few examples of their industrial applications include the deposition of a catalytic material inside the monolithic structure of particulate matter filters in automotive exhaust gas aftertreatment (Blažek et al., 2021; Isoz et al., 2022), sedimentation (Qi et al., 2008), or fluidization (Kang et al., 2019). Consequently, there exists a wide range of methods for their simulations with resolution ranging from the particle-resolved direct numerical simulation (PR-DNS) (Isoz et al., 2022), towards simplified two-fluid models in which both the fluid and the solid phase are treated as interpenetrating continua and their mutual interaction is modeled using (semi-)empirical closures (Municchi et al., 2019; Chauchat et al., 2017).

While the two-fluid models allow for large-scale simulations, the advantage of PR-DNS lies in its high fidelity. The high-fidelity of PR-DNS stems from the fact that the flow is solved with standard methods of computational fluid dynamics (CFD) with particles included into the fluid domain using a variant of the immersed boundary method, see, e.g., (Peskin, 2002) and (Mittal and Iaccarino, 2005). Consequently, no empirical closure is needed to compute the fluid forces acting on submerged particles. Furthermore, the complete flow field is simulated and no phenomenological turbulence models are required.

In PR-DNS, the particles themsevels are accounted for via the discrete element method (DEM), the description of which may be found in (Luding, 2008), as such, PR-DNS is a representative of the so-called

[*] Ing. Martin Isoz, Ph.D.: Institute of Thermomechanics, Czech Academy of Sciences, Dolejškova 1402/5; 182 00, Prague; CZ (ITCAS), and Department of Mathematics, Informatics, and Cybernetics, University of Chemistry and Technology, Technická 5; 166 28, Prague; CZ (DMICUCT), isozm@it.cas.cz
[**] Bc. Lucie Kubíčková: ITCAS, and DMICUCT
[***] Ing. Martin Kotouč Šourek: Department of Chemical Engineering, UCT, Technická 5; 166 28, Prague; CZ (DCEUCT)
[†] Ing.Ondřej Studeník: ITCAS, and DCEUCT
[‡] Bc. Anna Kovárnová: ITCAS, and DMICUCT

ISSN: 1805-8256, doi: 10.21495/em2023-27

CFD-DEM methods. Provided that the used DEM variant allows for treatment of arbitrarily shaped particles, i.e., fully resolves the particles geometry, the only approximations in PR-DNS originates in the assumption of particles rigidity and approximate handling of the solid-solid contact. For reviews of recent progress in DEM and CFD-DEM for non-spherical particles, the reader is refered to (Feng, 2023; Ma et al., 2022), respectively.

In the present work, we will concern ourselves with our custom PR-DNS variant (Isoz et al., 2022), in which the flow is solved using the standard segregated approach by Patankar and Spalding (1972) and Demirdzic et al. (1993), albeit modified similarly as in Blais et al. (2016). The solid phase is included in the flow via a hybrid fictitious domain-immersed boundary method (Municchi and Radl, 2017, 2018). The movement of particles is simulated utilizing the soft variant of DEM, that is, a variant allowing for overlaps between otherwise rigid solids and scaling the contact forces and torques according to the overlap magnitude. The specific used DEM is applicable to simulations of movement of arbitrarily-shaped solids and the used contact model is based on the work of Chen (2012), where the particle-particle overlap is measured via the overlap volume. Finally, adopting the terminology of Ma et al. (2022) for classification of DEM methods based on the approach to the particle surface definition; in our case, the particle shape is defined via a polyhedron-based model, which should be the most accurate (and most costly) from the currently available approaches. The complete model is implemented in the open-source C++ library OpenFOAM (OpenCFD, 2007) and is freely available from (Kotouč Šourek et al., 2023).

2. Simulation framework fundamentals

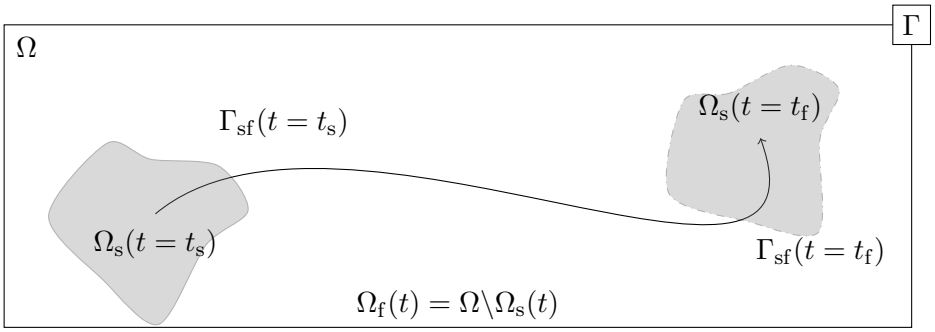

Fig. 1: Solution domain Ω and its division into Ω_{s}, Ω_{f} and Γ_{sf} at two different times $t = t_{\mathrm{s}}$ and $t = t_{\mathrm{f}}$. Trajectory of Ω_{s} in Ω is indicated by a dash-dotted line.

Let $\Omega \subset \mathbb{R}^3$ be a connected open domain with boundary $\Gamma = \partial\Omega$. Let Ω be split as $\Omega = \Omega_{\mathrm{s}} \cup \Omega_{\mathrm{f}} \cup \Gamma_{\mathrm{sf}}$, where Ω_{s} represents the part occupied by a solid phase, Ω_{f} the part occupied by a fluid and $\Gamma_{\mathrm{sf}} = \partial\Omega_{\mathrm{s}} = \partial\Omega_{\mathrm{f}}$ is the solid-fluid interface. When the solids present in Ω are moving, Ω_{s}, Ω_{f} and Γ_{sf} depend on time. Furthermore, for the case of a solid phase dispersed in Ω, Ω_{s} and Ω_{sf} may not be connected. The situation is illustrated in Fig. 1.

In Ω, we aim to solve momentum and mass balances for both the fluid and solid phase. Furthermore, as stated in Introduction, the fluid phase is solved within the standard CFD framework, while the solid phase movement is computed using DEM, and the two approaches are linked via an IBM variant.

Consequently, the complete $\Omega = \Omega_{\mathrm{s}} \cup \Omega_{\mathrm{f}} \cup \Gamma_{\mathrm{sf}}$ is taken into account for the fluid flow solution, and assuming an incompressible flow of a Newtonian fluid, the fluid flow governing equations are,

$$\begin{aligned} \mathcal{M}(\boldsymbol{u}) &= -\nabla\tilde{p} + \boldsymbol{f}_{\mathrm{ib}} \\ \nabla\cdot\boldsymbol{u} &= 0 \end{aligned}, \quad \mathcal{M}(\boldsymbol{u}) = \frac{\partial\boldsymbol{u}}{\partial t} + \nabla\cdot(\boldsymbol{u}\otimes\boldsymbol{u}) - \nabla\cdot(\nu\nabla\boldsymbol{u}) \tag{1}$$

where $\boldsymbol{u}$ is the fluid velocity, ν the kinematic viscosity, and $\tilde{p}$ the kinematic pressure. The forcing term $\boldsymbol{f}_{\mathrm{ib}}$ is calculated so that it generates a fictitious representation of Ω_{s} within Ω. This approach is known as a hybrid fictitious domain-immersed boundary method (Municchi and Radl, 2017, 2018; Isoz et al., 2022), a representative of the discrete forcing methods.

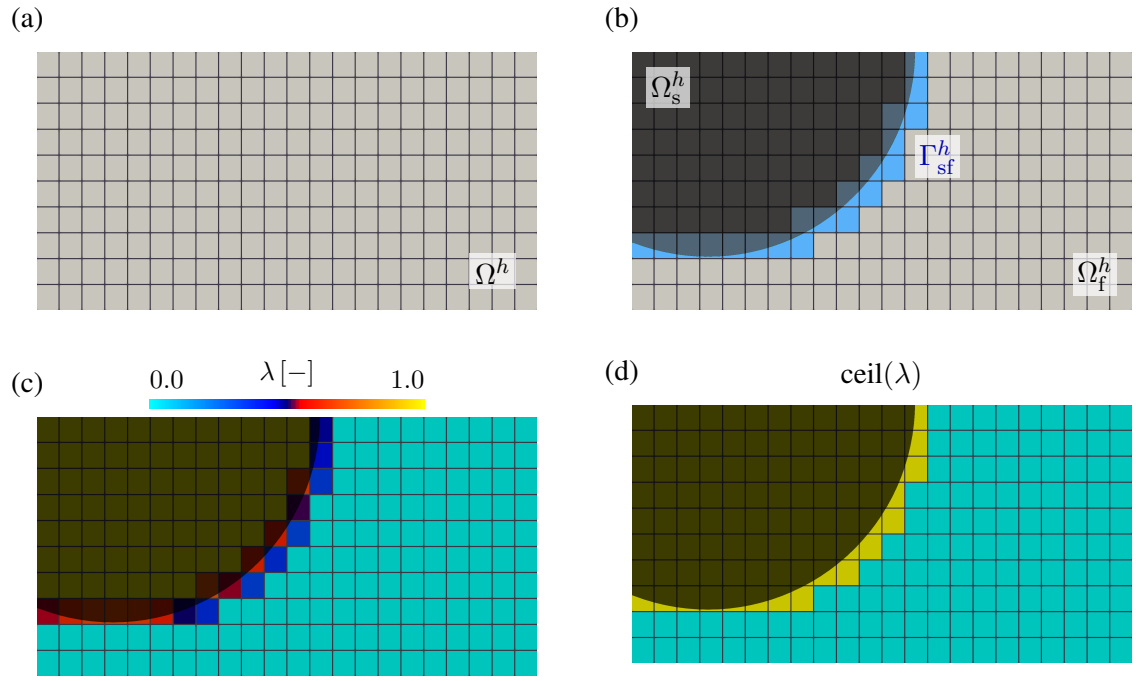

Fig. 2: (a) Finite volume mesh Ω^h. (b) Solid body $\mathcal{B}$ projected on Ω^h with diffuse discrete solid-fluid interface Γ^h_{sf}. (c) Resulting λ field. (d) Illustration of the ceiling function used in (2)*. Image adapted from (Kubíčková and Isoz, 2023).*

The additional forcing term $\boldsymbol{f}_{\mathrm{ib}}$ in (1) is based on the so-called λ field indicating the position of Ω_{s} in Ω and is defined as

$$\boldsymbol{f}_{\mathrm{ib}} = \mathrm{ceil}(\lambda)\tilde{\boldsymbol{f}}_{\mathrm{ib}}\,, \quad \tilde{\boldsymbol{f}}_{\mathrm{ib}} = \mathcal{M}(\boldsymbol{u}_{\mathrm{ib}}) + \nabla\tilde{p}\,, \quad \lambda = \begin{cases} 0 & \text{in} \quad \Omega_{\mathrm{f}} \\ 1 & \text{in} \quad \Omega_{\mathrm{s}} \\ \tilde{\lambda} \in (0,1) & \text{in} \quad \Gamma_{\mathrm{sf}} \end{cases} \tag{2}$$

where $\boldsymbol{u}_{\mathrm{ib}}$ is the flow velocity imposed inside Ω_{s}. Dividing Ω_{s} into individual solid bodies and marking a single body as $\mathcal{B}$, the imposed velocity $\boldsymbol{u}_{\mathrm{ib}}$ must be calculated so that the prescribed velocity boundary condition is fulfilled on $\Gamma^{\mathcal{B}}_{\mathrm{sf}}$ for all the bodies present in Ω.

In the used variant of the method, the forcing term $\boldsymbol{f}_{\mathrm{ib}}$ is constructed only after finite-volume discretization of (1). Projection of solid phase onto the finite volume mesh Ω^h and construction of the discrete $\boldsymbol{f}_{\mathrm{ib}}$ is illustrated in Fig. 2. The interface values of λ are computed based on the signed distance between the centroid of each $\mathcal{B}$ *surface cell* (in blue in Fig. 2b) and the $\mathcal{B}$ surface (Isoz et al., 2022).

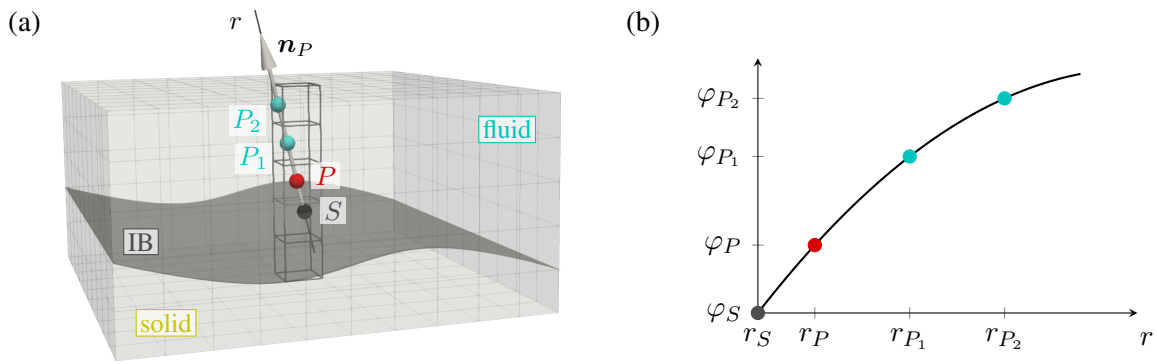

Fig. 3: (a) Interpolation points for a surface cell Ω^h_P. The points P_1 and P_2 are interpolation points located in Ω_{f} and S is a point at the $\mathcal{B}$ surface. (b) Example of a quadratic interpolation profile along the normal surface direction. Image adapted from (Kubíčková and Isoz, 2023).

For any intensive tensorial property φ, Dirichlet boundary conditions at $\Gamma^{\mathcal{B}}_{\mathrm{sf}}$, that is, at the surface of $\mathcal{B}$, are enforced by adjusting the values in the surface cells Γ^{h}_{sf}. In particular, second order polynomial approximation is used to estimate the value of φ at the centroid P (φ_P) of the surface cell Ω^h_P from the prescribed value in the surface point S (φ_S) and free-stream values in points P_1 (φ_{P_1}) and P_2 (φ_{P_2}) located at a line r passing through P and normal to S. The situation is illustrated in Fig. 3, for details see Isoz et al. (2022); Kubíčková and Isoz (2023).

The movement of individual solid bodies $\mathcal{B}_i$, $i = 1, \ldots, \mathrm{nSolids}$ is solved within the Lagrangian framework, using a soft variant of the discrete element method. The Newton's equations of motions for $\mathcal{B}_i$ are

$$m_i \frac{\mathrm{d}^2 \boldsymbol{x}_i}{\mathrm{d}t^2} = \boldsymbol{f}_{\mathrm{g}} + \boldsymbol{f}_{\mathrm{d}} + \boldsymbol{f}_{\mathrm{c}}\,, \quad I_i \frac{\mathrm{d}\boldsymbol{\omega}_i}{\mathrm{d}t} = \boldsymbol{t}_{\mathrm{d}} + \boldsymbol{t}_{\mathrm{c}}\,, \tag{3}$$

where m_i stands for the mass of $\mathcal{B}_i$ and $\boldsymbol{x}_i(t)$ for its center of mass position at time t, $\boldsymbol{\omega}_i$ is the body angular velocity and I_i is the matrix of its inertial moments. On the right hand side of $(3)_1$, $\boldsymbol{f}_{\mathrm{g}} = m_i \boldsymbol{g}(1 - (\rho_{\mathrm{f}}/\rho_{\mathrm{s}}))$ is the gravity/buoyancy force, $\boldsymbol{f}_{\mathrm{d}}$ is the drag force obtained by integrating $\boldsymbol{f}_{\mathrm{ib}}$ over surface cells of $\mathcal{B}_i$ and $\boldsymbol{f}_{\mathrm{c}}$ is the contact force. In $(3)_2$, $\boldsymbol{t}_{\mathrm{d}}$ and $\boldsymbol{t}_{\mathrm{c}}$ denote the drag and contact torques, respectively.

The treatment of contact will be illustrated on computation of normal contact force acting between solids $\mathcal{B}_i$ and $\mathcal{B}_j$, hereafter marked $\boldsymbol{f}^{\mathrm{n}}_{\mathrm{c}}$. The $\boldsymbol{f}^{\mathrm{n}}_{\mathrm{c}}$ computation is based on the work of Chen (2012), with particle-particle overlap scaled by the overlap volume V^{o}_{ij}, and reads as

$$\boldsymbol{f}^{\mathrm{n}}_{\mathrm{c}} = \left(\frac{Y_{ij} V^{\mathrm{o}}_{ij}}{L^{\mathrm{c}}_{ij}} + \gamma^{\mathrm{n}}_{ij} \sqrt{\frac{Y_{ij} M^{\mathrm{red}}_{ij}}{(L^{\mathrm{c}}_{ij})^3}} \frac{\partial V^{\mathrm{o}}_{ij}}{\partial t} \right) \boldsymbol{n}_{\mathrm{c}}\,, \tag{4}$$

where $\boldsymbol{n}_{\mathrm{c}}$ is the contact normal vector, Y_{ij} and $\gamma_{ij,\mathrm{n}}$ are the characteristic Young's modulus and normal damping coefficient, respectively, L^{c}_{ij} is the contact characteristic length, and M^{red}_{ij} is the reduced mass. The contact parameters Y_{ij}, γ^{n}_{ij}, L^{c}_{ij} and M^{red}_{ij} are computed as harmonic averages of the individual solids properties, which corresponds to damped springs in series.

The model (4) is particularly sensitive to the accuracy of V^{o}_{ij} and $\boldsymbol{n}_{\mathrm{c}}$. While it is possible to compute these utilising directly the finite volume mesh Ω^h as described in Isoz et al. (2022), the sensitivity of (4) to V^{o}_{ij} leads to either unrealistic demands on Ω^h resolution or to insufficient $\boldsymbol{f}^{\mathrm{n}}_{\mathrm{c}}$ accuracy (Studeník et al., 2022).

Altogether, the presented PR-DNS method provides a tool for detailed studies of small-scale systems, i.e., of fairly dilute laminar or almost laminar suspension flow. To increase the method applicability to real-life situations, we are currently focusing on three, below presented, research areas: (i) implementation of phenomenological turbulence models to enable PR-large eddy simulation (PR-LES) or even PR-Reynolds-averaged simulation (PR-RAS) of suspension flow, (ii) increasing contact solution efficiency to facilitate simulations of suspension flows with particle fractions approaching the closely packed bed, and (iii) development of methods of a-posteriori model order reduction to speed-up evaluation of parametric studies or optimizations.

3. Immersed boundary method and turbulence models

Two main approaches were considered to couple our PR-DNS solver with phenomenological turbulence modeling, PR-LES and PR-RAS. The PR-LES approach is closer to the actual flow physics. Compared to PR-RAS, PR-LES is (i) closer to the actual flow physics, (ii) computationally more costly, and (iii) easier to implement. Thus, we started with PR-RAS and the current implementation of turbulence covers the standard two-equation models, namely the k-ω, k-ε, k-ω SST and realizable k-ε models were implemented with wall functions for k, ω and ε.

The governing equations used are the Reynolds averaged variant of equations (1) with the Boussinesq hypothesis applied,

$$\begin{aligned} \mathcal{M}(\boldsymbol{u}) &= -\nabla \hat{p} + \boldsymbol{f}^{\mathrm{t}}_{\mathrm{ib}} \\ \nabla \cdot \boldsymbol{u} &= 0 \end{aligned}\,, \qquad \begin{aligned} \mathcal{M}(\boldsymbol{u}) &= \frac{\partial \boldsymbol{u}}{\partial t} + \nabla \cdot (\boldsymbol{u} \otimes \boldsymbol{u}) - \nabla \cdot [(\nu + \nu_t) \nabla \boldsymbol{u}] \\ \boldsymbol{f}^{\mathrm{t}}_{\mathrm{ib}} &= \alpha_{\boldsymbol{u}}(\lambda)\, [\, \mathcal{M}(\boldsymbol{u}_{\mathrm{ib}}) + \nabla \hat{p}\,] \end{aligned}\,, \tag{5}$$

where $\hat{p}$ is the turbulent pressure and ν_t the turbulent viscosity. The force term $\boldsymbol{f}^{\mathrm{t}}_{\mathrm{ib}}$ is similar to $\boldsymbol{f}_{\mathrm{ib}}$ from (2) with the ceiling function substituted by an $\alpha_{\boldsymbol{u}}$ field allowing for an adaptive boundary layer modeling, cf. Fig. 2d and Fig. 4b.

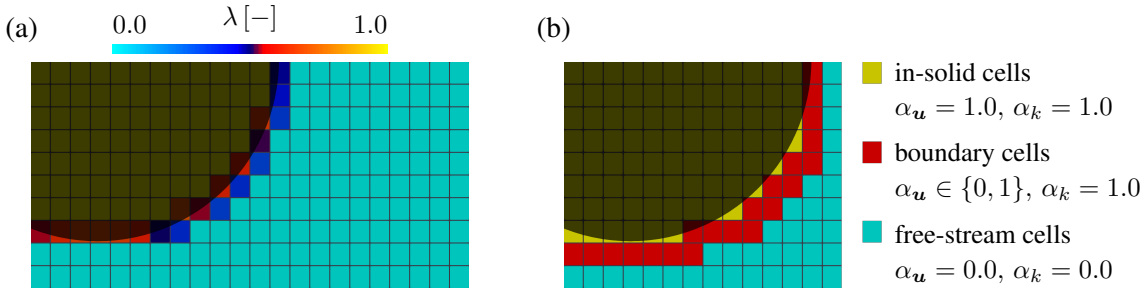

Fig. 4: (a) λ field from Fig. 2c. (b) λ-based cell division with values of the α fields.

The equations (5) are supplemented by the turbulence model equations in the form

$$\begin{aligned} \mathcal{N}(k) = S_{\mathrm{ib}}, \qquad & \nabla \cdot (\boldsymbol{u}\,\omega) = \nabla \cdot \left[\left(\nu + \frac{\nu_t}{\sigma_{\omega_1}}\right) \nabla\omega\right] + S^{\omega}\,, \\ \mathcal{N}(k) = \nabla \cdot (\boldsymbol{u}\,k) - \nabla \cdot \left[\left(\nu + \frac{\nu_t}{\sigma_{k_1}}\right) \nabla k\right] - S^{k}, \qquad & S_{\mathrm{ib}} = \alpha_k(\lambda)\,\mathcal{N}(k_{\mathrm{ib}})\,, \end{aligned} \tag{6}$$

where k is the turbulence kinetic energy, ω the specific rate of dissipation of k and the rest of the symbols represent model constants. Similarly to the momentum equation, the k conservation equation was extended by a source term S_{ib} to account for the presence of the solid body and to enforce boundary conditions for k by imposing k_{ib} in cells with non-zero α_k, see Fig. 4b. Boundary conditions for ω are enforced by imposing ω_{ib} values via a direct manipulation of the discretization matrix.

The values prescribed in the in-solid cells, see Fig. 4b, are simply set as $\boldsymbol{u}_{\mathrm{ib}} = \boldsymbol{0}$, $k_{\mathrm{ib}} = 0$, $\omega_{\mathrm{ib}} = \max(\omega^{\mathrm{old}})$. In the boundary cells, the ω_{ib} are computed via wall functions in forms reported by Kalitzin et al. (2005). The values of k_{ib} are reconstructed via interpolation between values at the solid surface obtained from wall functions and values in the free-stream. For low normalized distance to the wall (y^+), the used interpolation is, similarly to the laminar code version, quadratic polynomial. For high y^+ values, a logarithmic interpolation is applied. Also, the imposed velocity values are computed via quadratic interpolation which is, however, used only for low y^+. In cells with high y^+, the $\alpha_{\boldsymbol{u}}$ is set to be zero and the near-wall velocity behavior is governed by ν_t.

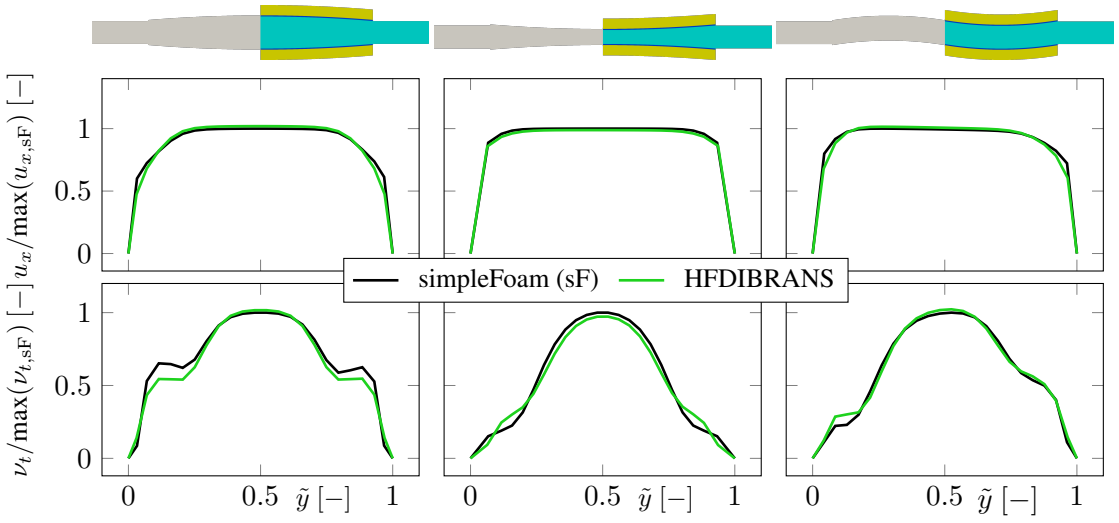

Fig. 5: Comparison of transversal velocity and turbulent viscosity profiles from simulations run with $\mathrm{Re} = 10^6$ *on bent geometries that are depicted at the top.*

The PR-RAS is in early development and up to now, it was verified on test cases with simple geometries and compared against simulations with geometry-conforming meshes run in simpleFoam (OpenCFD, 2007). In Fig. 5, there are depicted transversal velocity and turbulent viscosity profiles in flows with high Reynolds number in bent pipes. Overall, the PR-RAS shows acceptable accuracy but further validation is required.

4. Efficient contact treatment for arbitrarily shaped solids

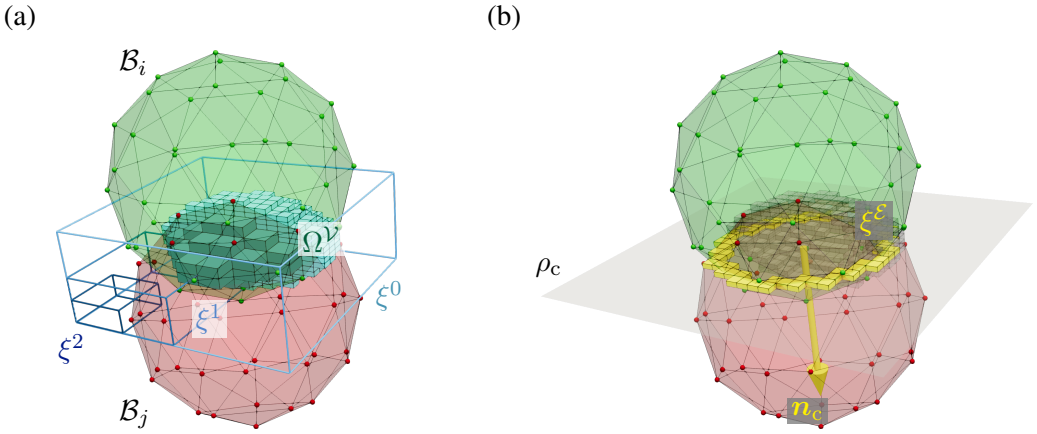

Fig. 6: Visualization of (a) virtual mesh ($\Omega^{\mathcal{V}}$) construction principle, (b) edge sub-volumes ($\xi^{\mathcal{E}}$), contact plane (ρ_c) and contact normal ($\boldsymbol{n}_c$) determination.

With the underlying finite volume mesh (Ω^h), the applied DEM variant is close to the level-set methods. However, the sensitivity of the contact model (4) to the accuracy of the overlap volume (V^o) computation leads to strict requirements for the resolution of the DEM computational mesh. In standard CFD codes, it is possible to adaptively refine Ω^h using the λ field, which indicates the positions of solid bodies in Ω^h. However, Ω^h is forced to carry all the data required by FVM, and its refinement is computationally costly. At the same time, most of these data are not required in the DEM part of the code.

To increase the efficiency of the code while maintaining the ability to work with arbitrarily shaped solids, we previously proposed an approach to complement a coarse (or flow-defined) FV mesh by a purely DEM *virtual* mesh localized only in the vicinity of possible or occurring contact (Studeník et al., 2022). Lately, the code was further improved by replacing a fixed virtual mesh discretization step by an R-Tree-based adaptive discretization.

R-Tree searching itself is a powerful algorithm for indexing and searching multi-dimensional data, such as spatial or geographical information (Guttman, 1984). The algorithm works by dividing the data into a hierarchy of hexahedra, where each node in the tree represents a bounding box that contains a subset of the data. This allows for efficient searching and retrieval of data that is spread out across multiple dimensions. In our implementation, R-Tree is used to efficiently detect and resolve contact between two geometry-defined solids.

To accurately compute V_{ij}^o for contact between the solids $\mathcal{B}_i$ and $\mathcal{B}_j$, we begin by constructing a hexahedron that represents the root node of the R-Tree. This hexahedron is formed as an intersection of the bounding boxes of the two solids, see ξ^0 in Fig. 6a. The R-Tree root is then divided into smaller hexahedra (sub-volumes) to search for all the overlapping areas between the two objects, see ξ^1 in Fig. 6a. If a sub-volume ξ^k does not intersect the boundary of $\mathcal{B}_i$ or $\mathcal{B}_j$ *and* it is not internal for *both* the bodies, it is discarded; see ξ^2 in Fig. 6a. A non-intersecting sub-volume internal for both $\mathcal{B}_i$ and $\mathcal{B}_j$is added to the total overlap volume V_{ij}^o. Finally, all the sub-volumes lying in side $\mathcal{B}_i$ and intersecting the surface of $\mathcal{B}_j$, or the other way around, are further refined. The resulting virtual mesh with maximum sub-volume refinement level $\ell_\xi = 5$ is marked $\Omega^{\mathcal{V}}$ and visualized in Fig. 6a.

In Fig. 6b, we show the edge sub-volumes $\xi^{\mathcal{E}}$ identified as R-Tree hexahedra intersecting surfaces of both $\mathcal{B}_i$ and $\mathcal{B}_j$ at the same time. Note that $\xi^{\mathcal{E}}$ always have the maximum allowed sub-volume refinement level. The edge sub-volumes are used to identify the contact plane (ρ_c) and to get the contact normal $\boldsymbol{n}_c$, which is crucial for $\boldsymbol{f}_c^n$ direction. Note that $\xi^{\mathcal{E}}$ do not usually lie perfectly in a single plane, as depicted in Fig. 6b. Consequently, the least-squares fit is used to obtain ρ_c.
Illustrative results of the R-tree-based virtual mesh approach are shown in Fig. 7. In the test, the solved contact is similar to the one shown in Fig. 6. In particular, we consider one pair of identical spherical particles projected onto a uniform hexahedral finite volume mesh with a resolution such that the particle diameter d_p spans over 20 FV cells. The top (green) sphere moves towards the stationary (red) sphere. The

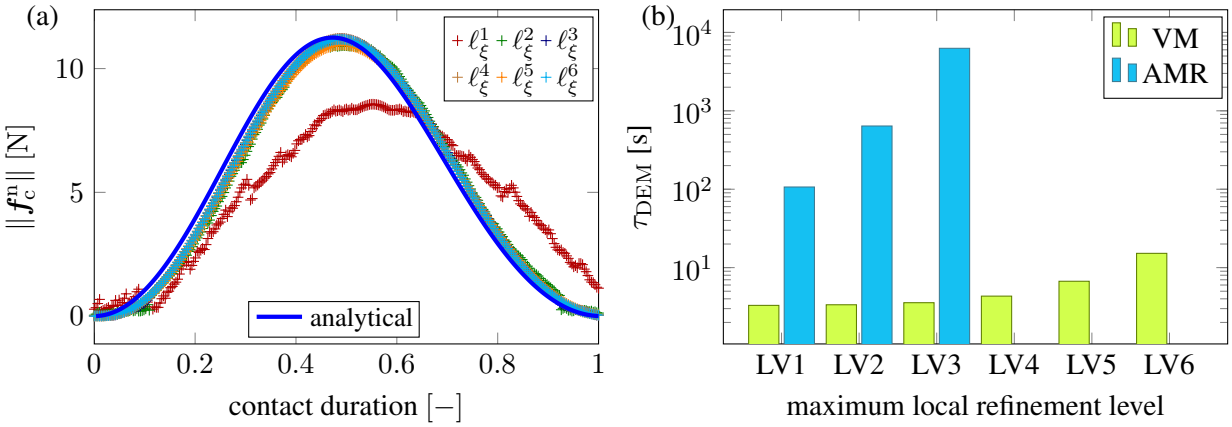

Fig. 7: Computation of normal contact force ($\boldsymbol{f}_c$) between two spheres. (a) Accuracy of $\|\boldsymbol{f}_c\|$ in dependence on the highest admissible local refinement level (LV). (b) Contact computing cost relative to contact between two perfect spheres for virtual mesh (VM) and adaptive CFD mesh refinement (AMR).

initial distance between the spheres is $1.5\,d_p$ and the initial velocity of the green sphere is $1\,\mathrm{m\,s^{-1}}$. Both spheres are considered to be of the same perfectly elastic material of $Y = 0.1\,\mathrm{GPa}$ and $\rho = 1000\,\mathrm{kg\,m^{-3}}$.

In Fig. 7a, we compare the accuracy of the contact normal force computation for different maximum allowed sub-volume refinement levels (ℓ_ξ^k, $k = 1, \ldots, 6$) to the analytical solution obtained for a contact between two perfect spheres. Note that for ℓ_ξ^3 the results are already (i) almost indistinguishable from the finest refinement ℓ_ξ^6, and (ii) close to the analytical solution.

The computing times required to obtain the solutions given in Fig. 7a are given in Fig. 7b. Furthermore, we compare the virtual mesh (VM) solution times to the times required when the adaptive mesh refinement (AMR) of the finite volume mesh is applied. All the shown times are scaled by the solution time of the contact between two perfect spheres, which leverages the geometric simplicity to compute V^o analytically. The AMR results were computed only up to ℓ_ξ^3, as higher refinement level were computationally unfeasible. Note that the computing times for ℓ_ξ^1, ℓ_ξ^2, and ℓ_ξ^3 are almost identical because the virtual mesh initialization requires more resources than the computation itself. For higher refinement levels ℓ_ξ^k, $k \geq 3$, the R-Tree based $\Omega^{\mathcal{V}}$ computational cost scale approximately as $k^{1.3}$.

5. Model order reduction

Even with the above outlined attempts to decrease the computational requirements of our particle-resolved CFD-DEM solver, these requirements still remain such that the solver is impractical for use in parametric studies or optimizations. However, computational costs of these two solver applications, i.e., parametric studies and optimizations, have been succesfully mitigated via methods of a-posteriori model order reduction (MOR) (Kahlbacher and Volkwein, 2007; Isoz, 2019).

Probably the most popular MOR approaches are based on a combination of the proper orthogonal decomposition (POD) by Pearson (1901) with Galerkin projection. Let us assume a physical system described by a transient partial differential equation (PDE). First, the PDE is spatially discretitized, e.g. by the finite volume method, to obtain a large system of ordinary differential equations, the full order model (FOM). Next, the FOM is (numerically) integrated in time to obtain an approximate solution of the original PDE.

Let $\{\boldsymbol{y}_i := \boldsymbol{y}(t_i)\}_{i=1}^n$ with $\boldsymbol{y}_i \in \mathbb{R}^m$ be the saved *snapshots* of the full order model with spatial resolution m. To perform POD-Galerkin model order reduction, the FOM snapshots are saved in a matrix of snapshots $Y = [\boldsymbol{y}_1, ..., \boldsymbol{y}_n] \in \mathbb{R}^{m \times n}$, where n is the number of available snapshots. Note that usually, $\mathrm{rank}\,(Y) = n$.

Afterwards, a low rank approximation of the matrix Y, marked Y^ℓ, is constructed via a truncated singular value decomposition of Y as

$$Y \approx Y^\ell = \Psi^\ell H^\ell,\ H^\ell = \Sigma^\ell \left(V^\ell\right)^{\mathrm{T}},\quad \Psi^\ell \in \mathbb{R}^{m \times \ell},\ \Sigma^\ell = \mathrm{diag}(\sigma_1, ..., \sigma_\ell) \in \mathbb{R}^{\ell \times \ell},\quad H^\ell \in \mathbb{R}^{\ell \times n}, \quad (7)$$

where Ψ^ℓ comprises the first ℓ stationary orthonormal spatial modes $\{\boldsymbol{\psi}_r\}_{r=1}^\ell$, *toposes*; and H^ℓ their corresponding time-dependent amplitudes $\{\boldsymbol{\eta}_r\}_{r=1}^\ell$, *chronoses*. In other words, $\boldsymbol{y}_i$ is approximated by a sum of

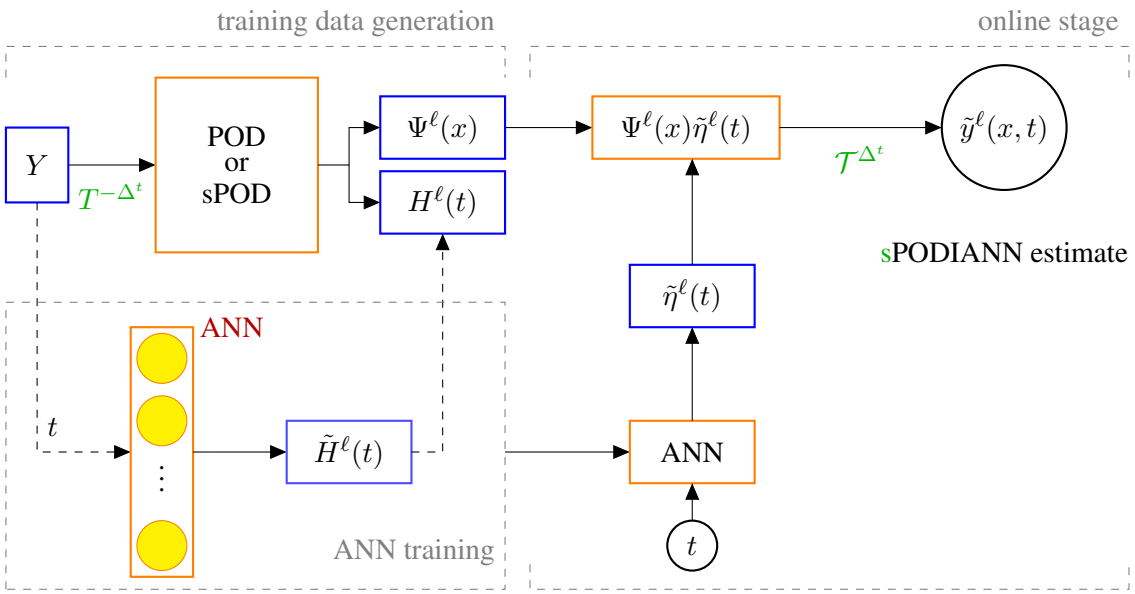

Fig. 8: PODIANN and sPODIANN framework architecture. The modifications required to replace POD by sPOD for time-dependent systems are given in green. Image from (Kovárnová et al., 2022)

the first ℓ dyadic pairs $(\boldsymbol{\psi}_r \otimes \boldsymbol{\eta_r})$, $r = 1, \ldots, \ell$. The number ℓ can be chosen based on the sought precision and the rate of decay of the singular values (σ_i) – the faster the decay, the more information is stored in the first modes.

Finally, the matrix Ψ^ℓ is used as a projector to construct the reduced order model (ROM) as

$$\begin{aligned} &\underline{\text{FOM}} && &&\underline{\text{ROM}} \\ &\dot{\boldsymbol{y}} = A\boldsymbol{y} + f(t,\boldsymbol{y})\,, && \xrightleftharpoons[\Psi^\ell]{(\Psi^\ell)^{\mathrm{T}}} && \dot{\boldsymbol{\eta}}^\ell = A^\ell\boldsymbol{\eta}^\ell + f^\ell(t,\boldsymbol{\eta}^\ell)\,, \\ &\forall t \in (0,T]\,,\ \boldsymbol{y}(0) = \boldsymbol{y}_0 && && \forall\, t \in (0,T], \quad \boldsymbol{\eta}^\ell(0) = \boldsymbol{\eta}_0^\ell \end{aligned} \tag{8}$$

$$\underline{\text{projection}}$$

$$A^\ell = \left(\Psi^\ell\right)^{\mathrm{T}} A\Psi^\ell, \quad f^\ell(t,\boldsymbol{\eta}^\ell) = (\Psi^\ell)^{\mathrm{T}} f(t, \Psi^\ell\boldsymbol{\eta}^\ell), \quad \boldsymbol{\eta}^\ell(0) = (\Psi^\ell)^{\mathrm{T}} y_0$$

Where $\boldsymbol{y}(t)$ and $\boldsymbol{\eta}^\ell$ are the original and the new variables, respectively; $A\boldsymbol{y}$ is the linear part of the original system and $f(t,\boldsymbol{y})$ comprises its non-linearity. Note that the new variable, $\boldsymbol{\eta}^\ell$, corresponds to the chronoses obtained from POD.

For transport-dominated systems such as those stemming from PR-DNS, the singular values decay tends to be extremely slow (Kovárnová et al., 2022). This renders construction of Y^ℓ via POD impractical as $\ell \to n$ is required to obtain an acceptable approximation. On the other hand, if one applies an operator $\mathcal{T}^{-\Delta^t}(y(t,x))$ to move the data into a frame of reference *co-moving* with the transport, the data become seemingly stationary and their POD-based approximation is, once more, efficient. While there exist multiple approaches to $\mathcal{T}^{-\Delta^t}$ definition, we have chosen to use the one by Reiss et al. (2018), called shifted POD (sPOD), that is able to treat systems with multiple different transports, (quasi-)optimally sort the data into individual frames of reference, apply the transport operators and reconstruct Y^ℓ as

$$Y^\ell = \sum_{k=1}^{N_{\mathrm{f}}} \mathcal{T}^{\Delta_k^t} \left(\sum_{r=1}^{\ell_k} \boldsymbol{\psi}_r^k \otimes \boldsymbol{\eta}_r^k \right) = \sum_{k=1}^{N_{\mathrm{f}}} \mathcal{T}^{\Delta_k^t} \left(\Psi_k^{\ell_k} H_k^{\ell_k} \right)\,, \tag{9}$$

where N_{f} is the number of frames of reference. Shifted POD requires information on the transports $\{\mathcal{T}^{-\Delta_k^t}\}_{k=1}^{N_{\mathrm{f}}}$ as an input in addition to Y, but that can be obtained directly from the above presented CFD-DEM solver.

Finally, for practical purposes it is necessary to have $\boldsymbol{y}^\ell$ available as a time-continuous mapping, which is traditionally achieved by the above-described Galerkin projection. However, using the sPOD disallows for Galerkin projection as no unique projector is available, cf. (8) and (9). Therefore, time-continuous $\boldsymbol{y}^\ell$

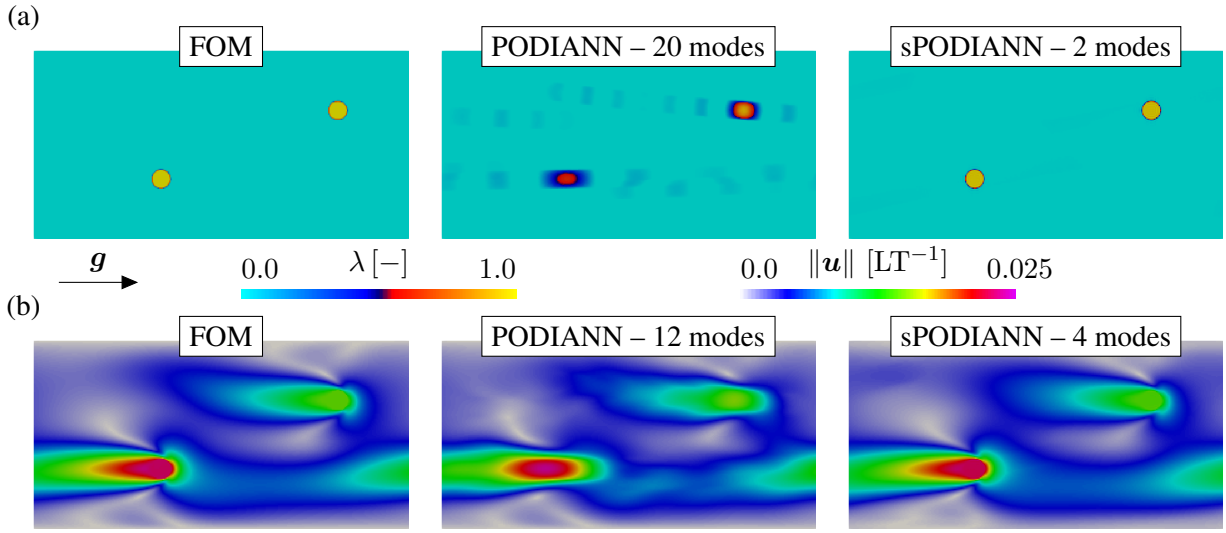

Fig. 9: Model order reduction of two falling discs, (a) qualitative view of the λ field at a given time, (b) qualitative view of the velocity field. Note the non-physical oscillations in PODIANN reconstructions, visible particularly in the case of the λ field, that stem from the inability of POD to capture transport.

needs to be found in another way – we have decided to use artificial neural networks as an interpolator between the known values stored in H^ℓ. The resulting method, shifted proper orthogonal decomposition with interpolation via artificial neural networks (sPODIANN), is outlined in Fig. 8.

The sPODIANN framework was applied to a simple two-dimensional system comprising two discs undergoing a gravity-driven motion through a rectangular periodic domain. The discs have the diameter $d_p = 0.001\,\mathrm{m}$ and are from materials with $\rho_1 = 1030\,\mathrm{kg\,m^{-3}}$, and $\rho_2 = 1060\,\mathrm{kg\,m^{-3}}$, respectively. The domain itself has dimensions $20\,d_p \times 10\,d_p$, is filled with a fluid of $\rho_\mathrm{f} = 1000\,\mathrm{kg\,m^{-3}}$ and $\nu_\mathrm{f} = 10^{-6}\,\mathrm{Pa\,s}$, and is discretized into 45000 FV cells (15 cells per d_p). In total, 601 evenly-spaced temporal snapshots are available for the ROM construction.

In Fig. 9, we compare the results of PODIANN (without transport operators) and sPODIANN frameworks. The approximation of the indicator λ field is shown in Fig. 9a, while the approximation of velocity is given in Fig. 9b. Note the wrong PODIANN λ field result obtained even for 20 POD modes, and the superior flow features resolution in the vicinity of the discs provided by sPODIANN.

6. Conclusions

In the present contribution, we outlined fundamentals of an in-house solver for particle-resolved direct numerical simulation (PR-DNS) of flows laden with arbitrarily-shaped particles. Afterwards, three different strategies to mitigate the extreme costs of PR-DNS were studied. In particular, we (i) examined the possibility to endow the used immersed boundary method variant with computationally cheap phenomenological turbulence modeling that provides a good agreement with results obtained on geometry-conforming meshes; (ii) presented an approach to treatment of contact between two geometry-defined solids capable of estimating the contact normal force close to the perfect sphere DEM with only four times its cost, and (iii) described a method for a-posteriori model order reduction applicable to PR-DNS-generated data. While all the shown results are only preliminary, they hint at the future potential of the presented methods.

Acknowledgments

The work was financially supported by the institutional support RVO:61388998 and by the Grant project with No. 22-12227S of the Czech Science Foundation

References

Blais, B., Lassaigne, M., Goniva, C., Fradette, L., and Bertrand, F. (2016) A semi-implicit immersed boundary method and its application to viscous mixing. *Computers & Chemical Engineering*, 85, pp. 136–146.

Blažek, M., Žalud, M., Kočí, P., York, A., Schlepütz, C. M., Stampanoni, M., and Novák, V. (2021) Washcoating of catalytic particulate filters studied by time-resolved x–ray tomography. *Chemical Engineering Journal*, 409, pp. 128057.

Chauchat, J., Cheng, Z., Nagel, T., Bonamy, C., and Hsu, T.-J. (2017) Sedfoam-2.0: a 3-d two-phase flow numerical model for sediment transport. *Geoscientific Model Development*, 10, 12, pp. 4367–4392.

Chen, J. (2012) *Understanding the Discrete Element Method: Simulation of Non-Spherical Particles for Granular and Multi-Body Systems*. PhD thesis.

Demirdzic, I., Lilek, Z., and Peric, M. (1993) A collocated finite volume method for predicting flows at all speeds. *Int. J. Num. Met. Fluids*, 16, 12, pp. 1029–1050.

Feng, Y. (2023) Thirty years of developments in contact modelling of non-spherical particles in DEM: a selective review. *Acta Mechanica Sinica*, 39, pp. 722343–1–722343–41.

Guttman, A. (1984) R-trees: A dynamic index structure for spatial searching. *SIGMOD Rec.*, 14, 2, pp. 47–57.

Isoz, M. (2019) POD-DEIM based model order reduction for speed-up of flow parametric studies. *Ocean Eng.*, 186, pp. 106083–1–106083–17.

Isoz, M., Kotouč Šourek, M., Studeník, O., and Kočí, P. (2022) Hybrid fictitious domain-immersed boundary solver coupled with discrete element method for simulations of flows laden with arbitrarily-shaped particles. *Computers & Fluids*, 244, pp. 105538–1–105538–22.

Kahlbacher, M. and Volkwein, S. (2007) Galerkin proper orthogonal decomposition for parameter dependent elliptic systems. *Disc. Math. Diff. Incl., Contr. Optim.*, 27, pp. 95–117.

Kalitzin, G., Medic, G., Iaccarino, G., and Durbin, P. (2005) Near-wall behavior of rans turbulence models and implications for wall functions. *Journal of Computational Physics*, 204, pp. 265–291.

Kang, X., Xia, Z., Wang, J., and Yang, W. (2019) A novel approach to model the batch sedimentation and estimate the settling velocity, solid volume fraction, and floc size of kaolinite in concentrated solutions. *Colloids and Surfaces A: Physicochemical and Engineering Aspects*, 579, pp. 123647.

Kotouč Šourek, M., Studeník, O., and Isoz, M. (2023) Implementation of the hybrid fictitious domain-immersed-boundary-discrete element method library in OpenFOAM. Available at https://github.com/MartinKotoucSourek/openHFDIB-DEM, 24.03.2023.

Kovárnová, A., Krah, P., Isoz, M., and Reiss, J. (2022) Shifted proper orthogonal decomposition and artificial neural networks for time-continuous reduced order models of transport-dominated systems. In Simurda, D. and Bodnar, T., eds, *Proceedings of the conference Topical Problems of Fluid Mechanics*, IT CAS, Prague, Czech Republic, pp. 111–118.

Kubíčková, L. and Isoz, M. (2023) On Reynolds-averaged turbulence modeling with immersed boundary method. *Topical Problems of Fluid Mechanics 2023*, pp. 104–111.

Luding, S. (2008) Introduction to discrete element methods. *European Journal Environmental and Civil Engineering*, 12, pp. 785–826.

Ma, H., Zhou, L., Liu, Z., Chen, M., Xia, X., and Zhao, Y. (2022) A review of recent development for the CFD-DEM investigations of non-spherical particles. *Powder Technology*, 412, pp. 117972–1–117978–62.

Mittal, R. and Iaccarino, G. (2005) Immersed boundary methods. *Annual Review of Fluid Mechanics*, 37, pp. 239–261.

Municchi, F., Nagrani, P. P., and Christov, I. C. (2019) A two-fluid model for numerical simulation of shear-dominated suspension flows. *International Journal of Multiphase Flow*, 120, pp. 103079–1–103079–15.

Municchi, F. and Radl, S. (2017) Consistent closures for euler-lagrange models of bi-disperse gas-particle suspensions derived from particle-resolved direct numerical simulations. *International Journal of Heat and Mass Transfer*, 111, pp. 171–190.

Municchi, F. and Radl, S. (2018) Momentum, heat and mass transfer simulations of bounded dense mono-dispersed gas-particle systems. *Int. J. Heat and Mass Trans.*, 120, pp. 1146–1161.

OpenCFD (2007) *OpenFOAM: The Open Source CFD Toolbox. User Guide Version 1.4, OpenCFD Limited*. Reading UK.

Patankar, S. and Spalding, D. (1972) A calculation procedure for heat, mass and momentum transfer in three-dimensional parabolic flows. *Int. J. of Heat and Mass Tr.*, 15, 10, pp. 1787–1806.

Pearson, K. (1901) On lines and planes closest fit to systems of points in space. *The London, Edinburgh, and Dublin Philosophical Magazine and Journal of Science*, 2, pp. 559–572.

Peskin, C. (2002) The immersed boundary method. *Acta Numerica*, 11, pp. 479–517.

Qi, X.-B., Zhu, J., and Huang, W.-X. (2008) A new correlation for predicting solids concentration in the fully developed zone of circulating fluidized bed risers. *Powder Technology*, 188, 1, pp. 64–72.

Reiss, J., Schulze, P., Sesterhenn, J., and Merhmann, V. (2018) The shifted proper orthogonal decomposition: a mode decomposition for multiple transport phenomena. *SIAM J. Sci. Comput.*, 40, pp. A1322–A1344.

Studeník, O., Kotouč Šourek, M., and Isoz, M. (2022) Octree-generated virtual mesh for improved contact resolution in CFD-DEM coupling. *Topical Problems of Fluid Mechanics 2022*, pp. 151–158.